High-Resolution, Anthropomorphic, Computational Breast Phantom: Fusion of Rule-Based Structures with Patient-Based Anatomy

by

Xinyuan Chen

Graduate Program in Medical Physics
Duke University

Date:_____
Approved:

_____
Joseph Yuan-Chieh Lo, Supervisor

_____
Lars Johannes L Grimm

_____
William Paul Segars

Thesis submitted in partial fulfillment of
the requirements for the degree of Master of Science
in the Graduate Program in Medical Physics
in the Graduate School
of Duke University

2017

ABSTRACT

High-Resolution, Anthropomorphic, Computational Breast Phantom: Fusion of Rule-Based Structures with Patient-Based Anatomy

by

Xinyuan Chen

Graduate Program in Medical Physics
Duke University

Date:_____

Approved:

_____
Joseph Yuan-Chieh Lo, Supervisor

_____
Lars Johannes L Grimm

_____
William Paul Segars

An abstract of a thesis submitted in partial
fulfillment of the requirements for the degree
of Master of Science in the Graduate Program in Medical Physics
in the Graduate School of
Duke University

2017

Copyright by
Xinyuan Chen
2017

Abstract

Patient based breast phantoms that are segmented from real human images have inherently high realism. However, they are limited by low resolution and low frequency components. In this study, patient-based phantoms were enhanced by combining with rule based breast structures, so that the hybrid phantoms have both high realism and high resolution.

Starting from the original phantoms segmented from a new cohort of 31 clinical breast CT images, 3D radially symmetric power-law noise (PLN) with β=3 was added at the boundary between adipose and glandular tissue to connect broken tissue and create a high frequency contour of the glandular tissue. Then, selected high-frequency features from the FDA rule-based computational phantom (Cooper's ligaments, ductal network, and blood vessels) were fused into the phantom.

The effects of each step of phantom enhancement were demonstrated by 2D mammography projections and digital breast tomosynthesis (DBT) reconstruction volumes. The addition of PLN and rule-based models leads to a continuous decrease in power exponent β. The final enhanced β is 2.80 ± 0.14 for simulated mammograms, and 1.84 ± 0.15 for DBT reconstructions. The Laplacian fraction entropy (LFE) curve calculated from mammograms of final enhanced phantom has maximum value around 120% and decays as frequency increases.

Both results from power spectrum analysis and LFE analysis agree with previous studies of real patients' images.

In this study, we demonstrated a new approach for creating hybrid computational breast phantoms that combine the inherent realism of patient-based anatomy as well as high resolution and quantitative control of mathematical textures and rule-based structures.

Dedication

To my mother, who is the best friend of my life, always supporting me generously and selflessly. And to my father who guides me with wisdom and gives me the freedom to explore myself, as well as the world, like a little bird in the sky.

Contents

List of Figures

Acknowledgements

I would like to thank my advisor, Dr. Joseph Lo, who inspired my interests of doing research with his extraordinary mentoring.

I would also like to thank Dr. Stephan Glick, Dr. Christian Graff, Dr. Craig Abbey, my lab mates Thomas Sauer, Gregory Sturgeon, Bibo Shi for their generous help, and invaluable advice.

1. Introduction

Early detection of breast cancer can avoid aggressive treatment such as mastectomy, and improve cure rates of breast cancer. Therefore, better diagnostic imaging techniques for breasts are in high demand. Currently, mammography is practiced as a primary method for screening, [1][2] however it is being gradually replaced by digital breast tomosythesis (DBT), as DBT can provide 3D breast volumes with the same dose and screening time as mammography. [3]–[7] Besides, many other technologies have been approved for clinical practice recently, such as contrast enhanced mammography, [8][9] contrast enhanced DBT and breast CT. [10]–[14] During the development of breast imaging techniques, computational breast phantoms have been widely used as a substitute for real patient breasts in testing newly developed imaging methods, for both practical reasons (i.e., large variety and low cost) and ethical reasons (i.e., no radiation risk). By providing the "known truth", computational breast phantoms can be used to evaluate image quality quantitatively. In addition, computational lesion models can be inserted into the virtual breast phantoms to evaluate lesion detectability and task-based optimization of imaging system parameters.

Currently, two types of computational breast phantoms have been developed. One is a rule-based phantom, which characterize all breast features through mathematical models. In 2002, Bakic *et al*. simulated breast phantoms with a distribution of large and medium scale tissue structures such as adipose compartments and ducts for the purpose of generating synthetic mammograms. [15]–[17] Lau *et al.* replaced the adipose compartments in Bakic's phantoms by binarized power-law noise to enhance realism. [18] Graff *et al.* reported on digital

breast phantoms with detailed structures such as a ductal tree, Cooper's ligaments, veins and arteries. [19] Others have also investigated rule-based phantoms for breast imaging. [20]–[26] The other approach is patient-based phantoms, which segment breast structures from real patient images. The initial patient based phantoms were generated by segmentation from breast CT of mastectomy specimens. [27], [28] Built upon the original work of Li *et al.*, [29] and improvements made by Segars *et al.*, [30] our lab previously developed a new set of breast phantoms based on *in vivo* patient CT data to represent a larger number of intact breasts. [31]

Although rule-based breast phantoms are more flexible and time-saving, patient-based phantoms have inherently higher realism. However, during the process of image acquisition, reconstruction, denoising, and segmentation, some of the finest details of breasts are lost in patient-based breast phantoms. In this study, patient-based breast phantoms that were segmented from in vivo breast CT images were combined with rule-based breast structures, such as high frequency glandular contour, Cooper's ligament, ductal system and vessel network. The goal of these new 'hybrid' phantoms is to retain the realism from breast CT images, while adding high frequency details from mathematical breast models.

2. Methods

2.1 Phantom development methods

2.1.1 Overview

The flowchart of the phantom enhancement of this study is shown in Figure 1. These steps are summarized briefly here, then elaborated upon in the following sections. Starting from the original phantoms that were segmented from breast CT (bCT) images, the phantoms were then finite element compressed into 4 atlas templates for skin boundaries corresponding to different thicknesses. [32][33] After that, binarized power-law noise was added at the boundary between adipose and glandular tissue to restore the high frequency contour of glandular tissue. Finally, computational breast structures from Graff *et al.*, [19] including Cooper's ligaments, ductal trees and vessel networks, were fused into the phantoms to further restore high frequency anatomical structures that are broken or lost after the segmentation process.

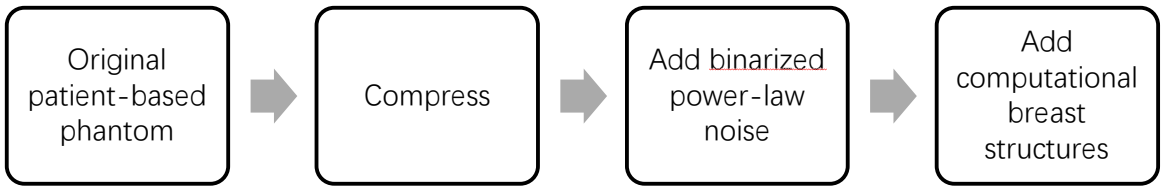

Figure 1: A flowchart for phantom generation.

2.1.2 Original phantoms

Previous studies from our group were all based on a first cohort of bCT cases with a voxel pitch of approximately 350 x 350 x 350 μm, which inherently limited the resolution of the resulting phantoms. [10], [31], [34], [35] For this study, 30 patient-based phantoms were generated from a new cohort of breast CT images. Theses phantoms were based on a new cohort of 140 patients acquired at the University of Massachusetts on a clinical breast CT system (Koning Corporation, West Henrietta, NY). These cases were reconstructed with filtered back projection (FBP) resulting in an isotropic voxel size of 155 x 155 x 155 μm. These clinical volumes were converted into voxelized phantoms through a process of denoising and segmentation similar to the previous cohort of cases. [28] For each phantom, six successive integers (1 to 6) were assigned according to bCT intensity, i.e., 1 represents pure adipose, 6 stands for skin mask, and 2 to 5 are for glandular tissue of increasing densities.

Finally, a previously published finite element technique [29,30] was used to compress the phantoms. This atlas-based compression scheme reduces computational cost and also provides consistent breast shape and size for numerical analysis. The phantoms were interpolated to have 77.5 x 77.5 x 77.5 μm voxel size during the compression process to avoid further loss of resolution, with the goal of producing a final voxel pitch comparable to that of clinical mammography or DBT systems.

Depending on their original mean thickness, the phantoms were compressed into one of four atlas templates from typical cases representing different thicknesses of the compressed

breast including 5, 6, 7, and 8 cm. Figure 2 shows some examples of the original compressed phantoms used in this study.

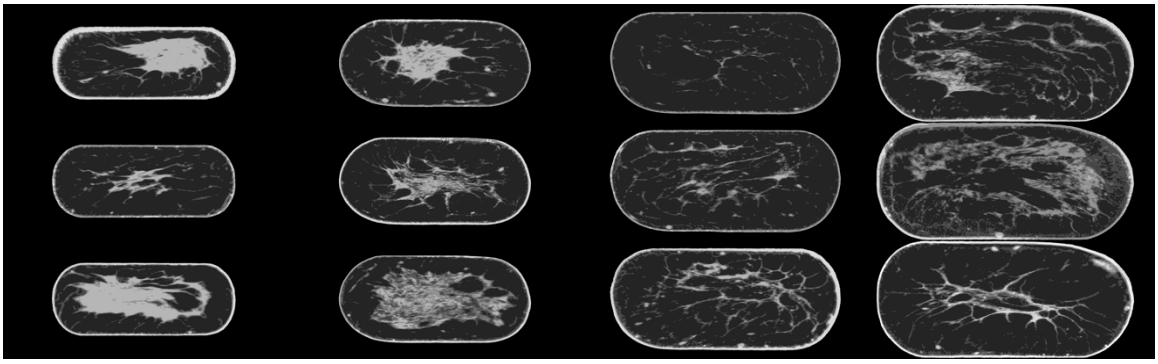

Figure 2: Coronal slices of original compressed patient-based breast phantoms, with thickness = 5cm, 6cm, 7cm, 8cm from left column to right column. These phantoms preserve the high realism and large diversity of human anatomy, but lack the high frequency anatomical details.

2.1.3 Power Law Noise

Three-dimensional, radially symmetric power law noise (PLN) with exponent β=3 was generated according to the observed power spectrum behavior of real mammogram images . [36] Unlike previous work that added PLN throughout all adipose regions, [18] PLN was added only within a boundary mask region between adipose and glandular tissue in order to connect broken glandular tissue and increase spatial high-frequency detail at the glandular contour. Specifically, this mask operated upon the boundary between the adipose tissue (class 1) and the lowest level of glandular tissue (class 2), where the faintest or smallest portions of glandular

tissue were most likely to be degraded during the phantom creation process. Figure 3 shows three ROIs from axial slices of the phantom before and after adding PLN.

Different parameters of PLN addition, including binarization threshold, boundary radius and minimum glandular volume, can be adjusted to reach different effects of phantom enhancement. As shown in figure 4(a), the binarization threshold is the percentage of maximum value of PLN. Values exceeding the threshold were set to the same value as the lowest level of glandular tissue (value=2), while values below the threshold were set to the value of adipose tissue (value=1). The boundary mask was defined by convolving the edge of the glandular tissue with a disk whose radius that can be changed, i.e., boundary radius. Thus, the boundary radius determines the width of the boundary region where PLN was added (figure 4(b)). Finally, the minimum glandular volume defines the minimum volume of glandular structures that would be considered for enhancement with PLN. Any glandular structure smaller than the minimum volume was considered either noise or artifact and excluded from the high frequency enhancement. In this study, a specific combination of the 3 parameters corresponding to a binarization threshold 85%, a boundary radius 5 voxel, and a minimum glandular volume of 50x50x50 voxel^3 were selected for further quantitative analysis.

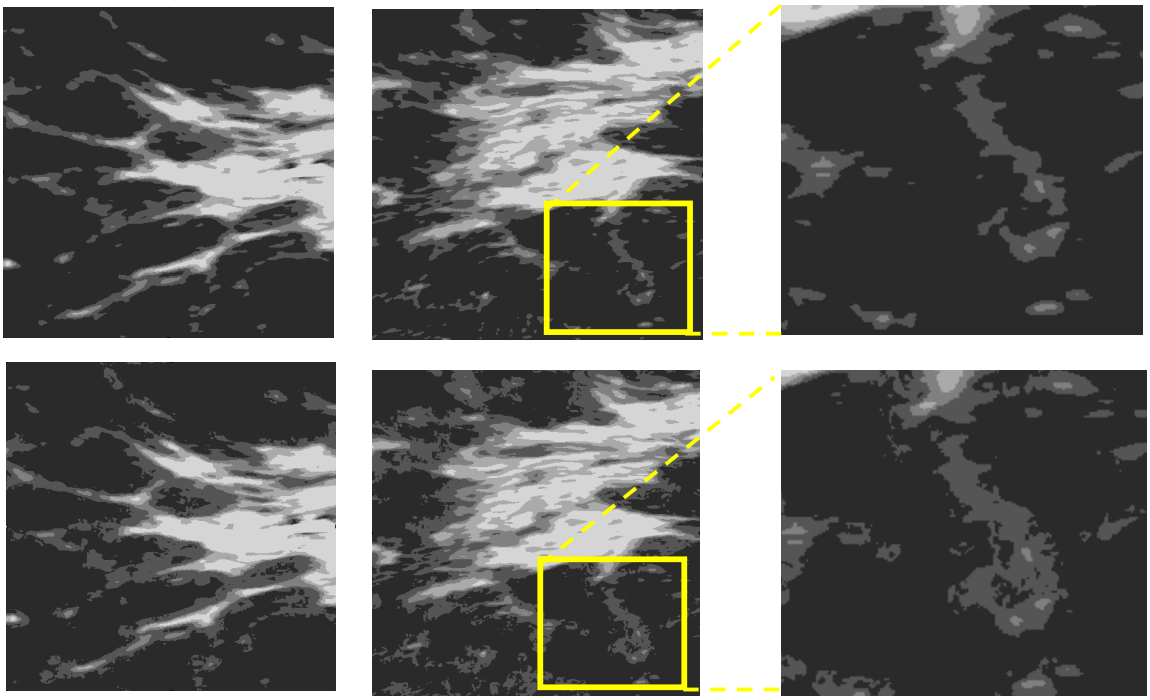

Figure 3: The effects of adding PLN. The first column shows ROIs from axial slices of the original compressed phantoms. The second column are the same ROIs with the addition of ß=3 PLN at the boundary of glandular tissue. The last column zooms in the region delineated by the yellow rectangles in the middle column.

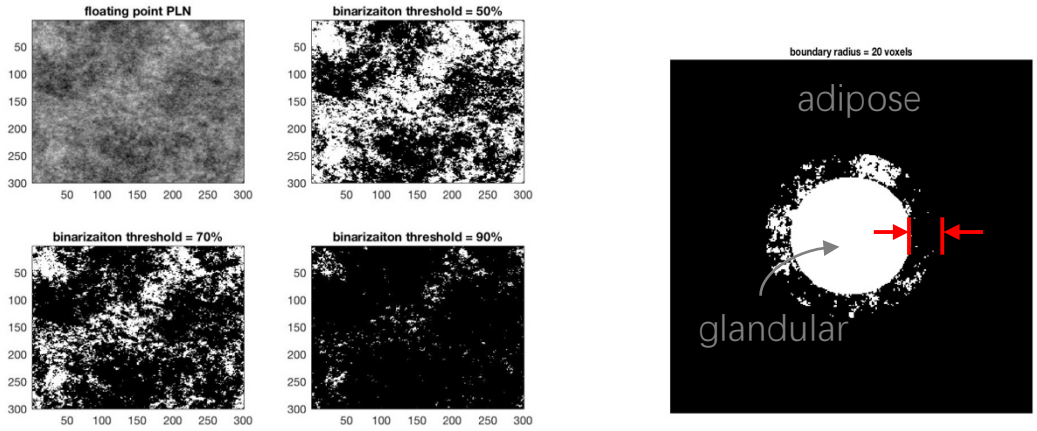

(a) (b)

Figure 4: Control of different power-law noise (PLN) parameters. (a) The upper-left figure shows the unbinarized PLN, followed by binarized PLN with increasing binarization threshold: 50%, 70%, and 90%. (b) Simplified diagram with white showing a round shape pure adipose, and dark representing the adipose region. PLN was added in the boundary mask with boundary radius equal to 20 voxels.

2.1.4 Cooper's Ligament, Ductal Network, and Blood Vessels

Computational structures were adopted from the rule-based phantom of Graff *et al.* [19] providing high-frequency details that were degraded or lost during the creation of the patient-based phantoms.

Cooper's ligaments are connective tissue in breast that originate from the chest wall, branch out through and around the breast tissue and terminate at the surface of the skin, supporting the breast's position and shape. [37] The ligaments were generated from Perlin-noise perturbed spheroids that enclose volumes on the order of 1 ml in adipose and glandular regions and were set to have 250-300 μm thickness around the boundary of the spheroids

according to breast anatomy. [38] Ductal networks that transport milk from glandular tissue to the nipple were simulated by a recursive random tree algorithm until the branches reached a minimum radius of 100 μm. A similar algorithm was applied to generate the vascular system growing from the chest wall with changes in parameters that control the length and curvature of the branches. 3D rendering of Cooper's ligaments, ductal networks and vascular systems as displayed in Figure 5. The high resolution rule-based structures were matched randomly with the compressed phantoms after their independent generation.

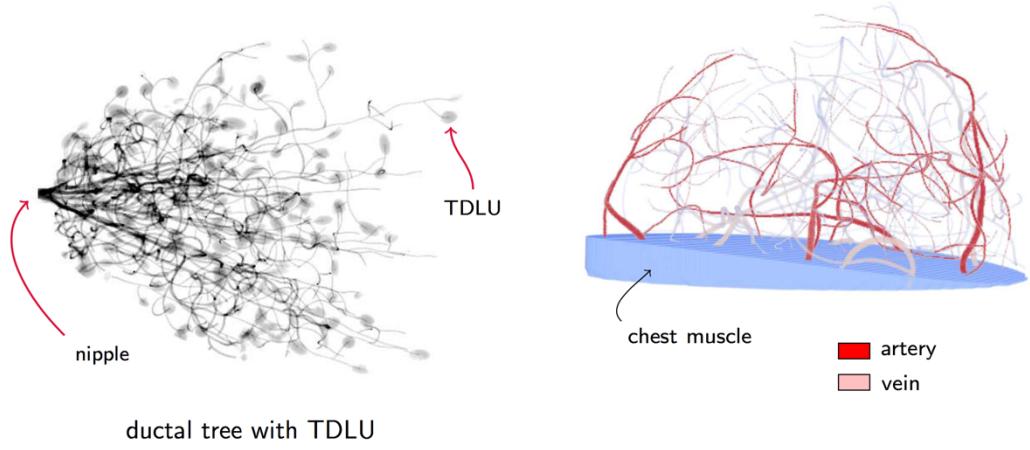

Figure 5: Projection and 3D rendering of brest structures. (a) projection image of a ductal network. (b) Vascular system originating form chest muscle layer (bottom). [19]

2.2 Quantitative Evaluation

Quantitative analysis was performed on the three phantom variants: the original phantoms, phantoms with PLN, and phantoms after complete enhancement (addition of PLN and rule-based details including Cooper's ligaments, ductal network, and blood vessels). For all

three phantom variants, simulated images were generated for both mammography and DBT using a previously reported projection and FBP reconstruction algorithm. [39] The resulting images were analyzed for anatomical realism using two techniques, power law slope and Laplacian fractional entropy.

2.2.1 Power spectrum analysis

Power spectra were calculated for simulated mammograms and DBT reconstructed volumes of ROIs of 46.5 x 46.5 mm^2 overlapping by 50% in both x and y directions were taken from mammograms and the middle slice of DBT volumes. The Hanning window was applied prior to the Fourier transformation to reduce the spectral leakage. Log-log plots of radially averaged power spectra versus frequency within the range of 0.2-1.0 mm^{-1} for mammograms, and 0.1-0.7 mm^{-1} for DBT slices were fitted linearly in order to calculate power exponent β.[40][41]

2.2.2 Laplacian fractional entropy (LFE) analysis

Laplacian fractional entropy analysis was implemented to characterize non-Gaussian statistical properties for simulated mammograms. [42] Firstly, the region of analysis was defined by an eroded skin mask that is 1 cm inside the original skin mask. Then Gabor filter with 1.4-octave bandwidth and 6 angles incremented by 1/6 pi was applied to the selected region. The outputs are similar to receptive fields in the early

visual cortex, which is particularly relevant to visually perceived structure in images. Subsequently, the histogram of all Gabor filter responses was fitted by Gaussian curve and Laplacian curve respectively through the maximum likelihood estimation function in MATLAB (Mathworks Inc., Natick MA). The relative entropy was calculated from the two fittings.

3. Results

3.1 Visual demonstration

Figure 6 shows simulated mammograms and reconstructed middle slices of DBT for one phantom case at each step of the enhancement, including the original phantom, with addition of power-law noise (PLN), and with both PLN and rule-based structures. These images visually demonstrate the addition of high frequency details and maintenance of high anatomical realism during the enhancement process.

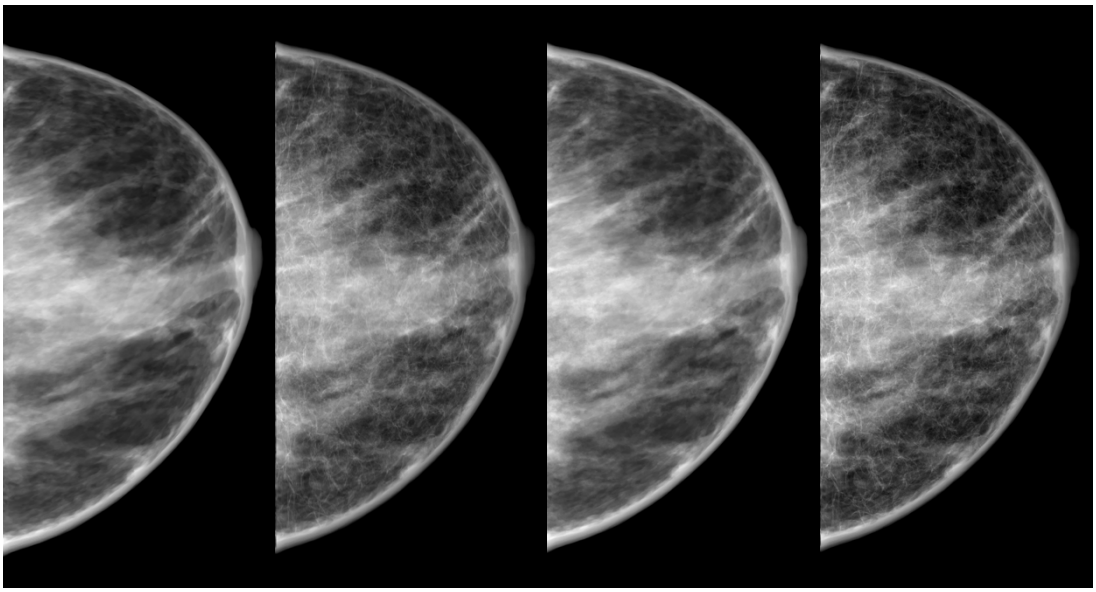

(i) 1a. original 1b. +PLN 1c. +Cooper 1d. +ducts/vessels

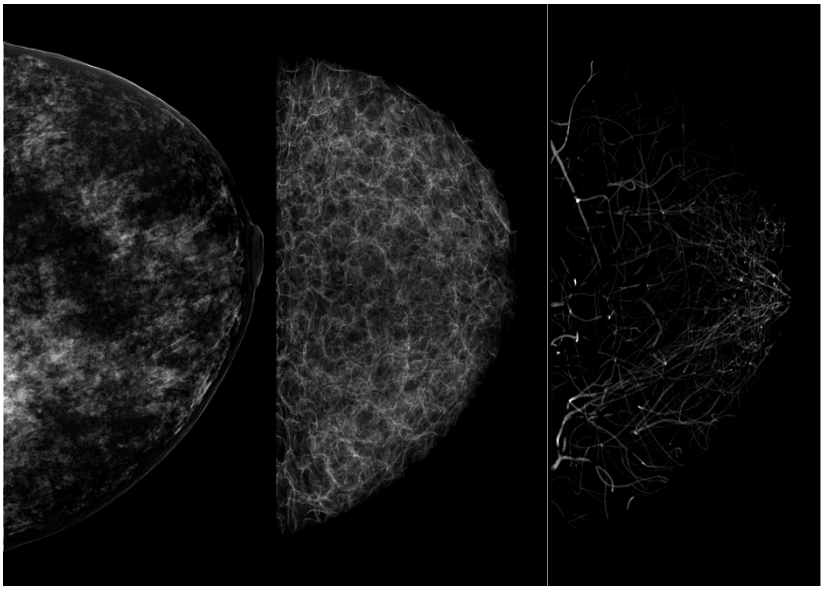

(ii) 2a=1b-1a(PLN) 2b=1c-1b(Cooper) 2c=1d-1c(ducts/vessels)

Figure 6-a: Simulated CC mammogram of each step of phantom enhancement. (Row i) From left to the right are original phantom (1a), followed by addition of PLN (1b), Cooper's ligaments (1c), and ducts and vessels (1d). (Row ii), Difference image corresponding to each of two steps shown in (i).

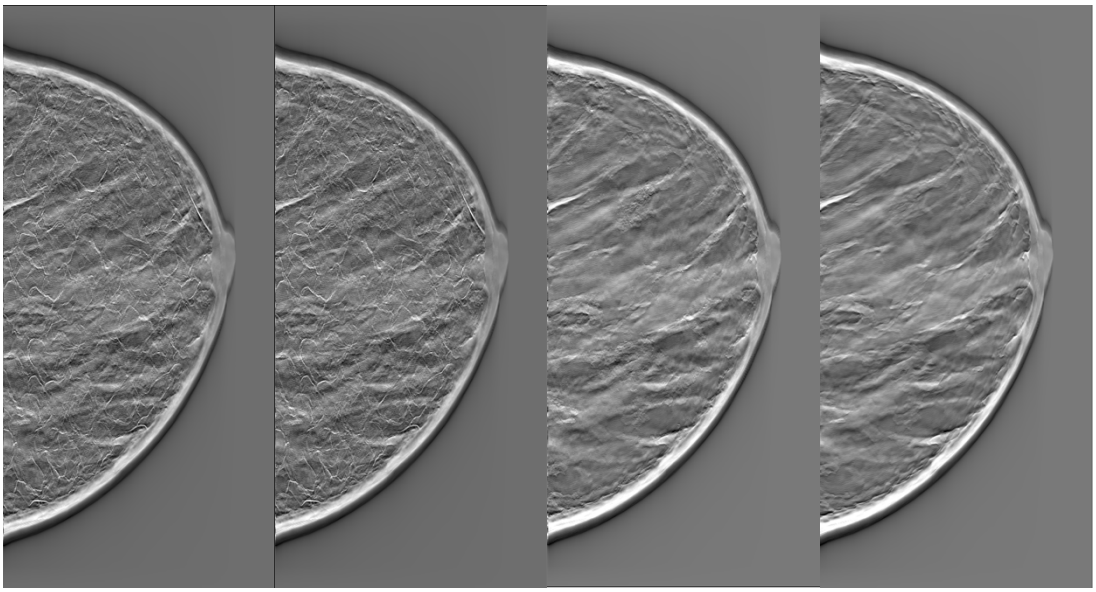

(i) 1a. original 1b. +PLN 1c. +Cooper 1d. +ducts/vessels

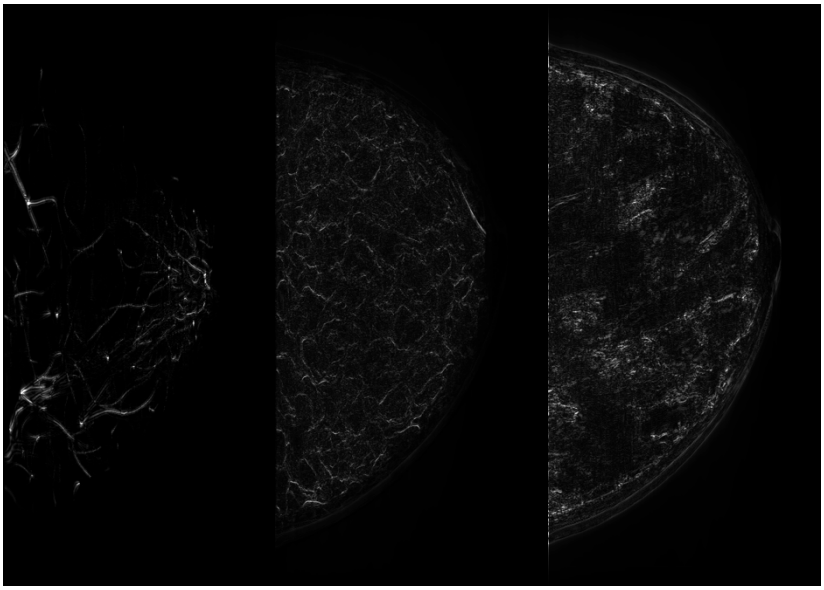

(ii) 2a=1b-1a(PLN) 2b=1c-1b(Cooper) 2c=1d-1c(ducts/vessels)

Figure 6-b: Middle slice of DBT reconstructed images at each step of the enhancement. (Row i) From left to right, DBT reconstruction of the original phantom (1a), phantom with PLN (1b), phantom with PLN, Cooper's ligaments (1c), ducts, and vessels (1d). (ii) The difference of DBT reconstructions between each step shown in (i).

3.2 Effects of power-law noise (PLN) parameters

Figure 7 and figure 8 demonstrate the effects of increasing PLN boundary radius and PLN binarization threshold respectively. Each row shows the same 39x39 mm^2 (500x500 $pixel^2$) ROIs taken from simulated mammograms. In Figure 7, the amount of PLN increased as boundary radius increased from 0 voxel to infinity, i.e., PLN was added throughout all adipose regions without being limited to the boundary region between adipose and glandular tissue. In Figure 8, the amount of binarized PLN being added decreased as binarization threshold increased from 0% to 100%, which affects the frequency and texture of the additional PLN.

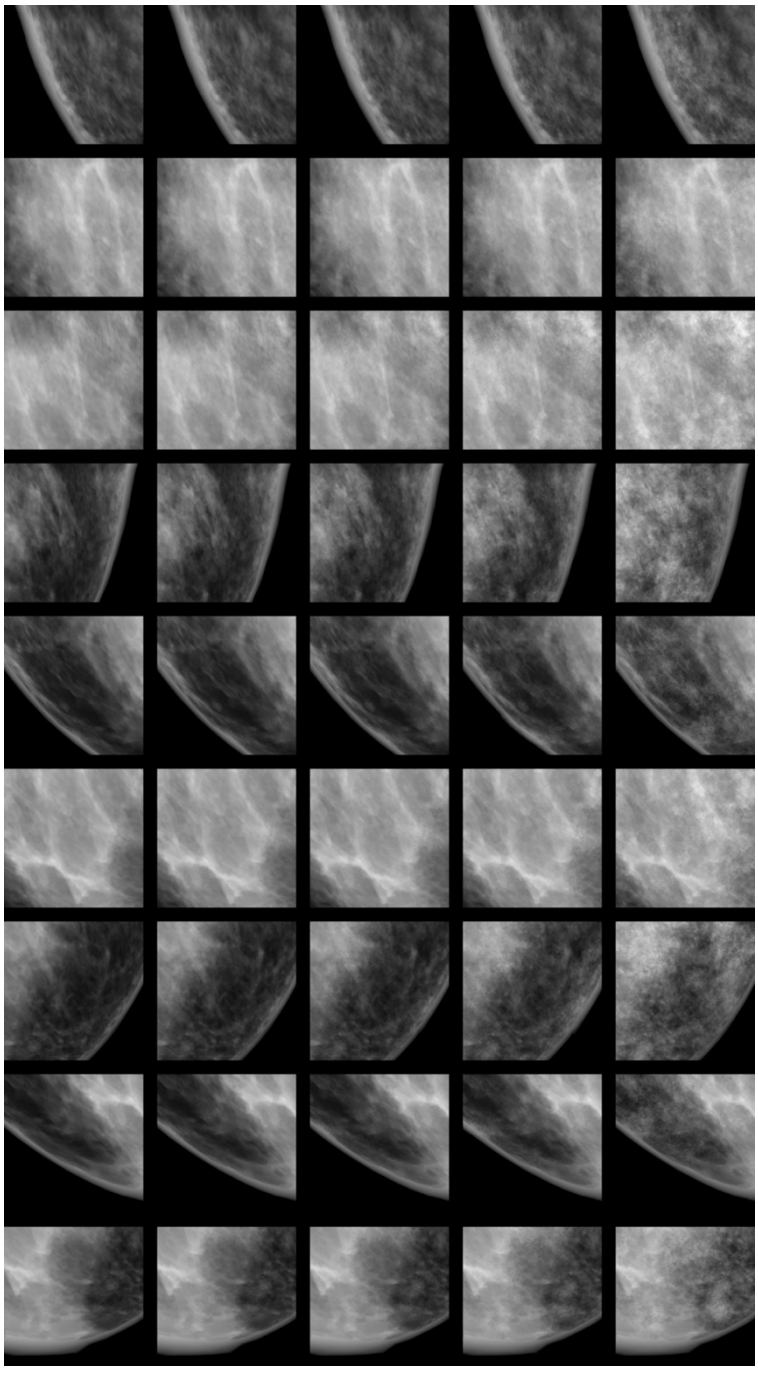
ROI1
ROI2
ROI3
ROI4
ROI5
ROI6
ROI7
ROI8
ROI9
R=0
R=3
R=5
R=10
R=Inf

Figure 7: Effects of boundary radius using 9 ROIs from one phantom. Each row shows the same ROI of X-ray projections with increasing PLN boundary radius (R) in the unit of voxels. Radius=0 means no PLN was added, i.e., the original phantom, while radius=Inf means PLN was not limited by the boundary, but was added everywhere within the adipose region. The amount of PLN added increased from left to right.

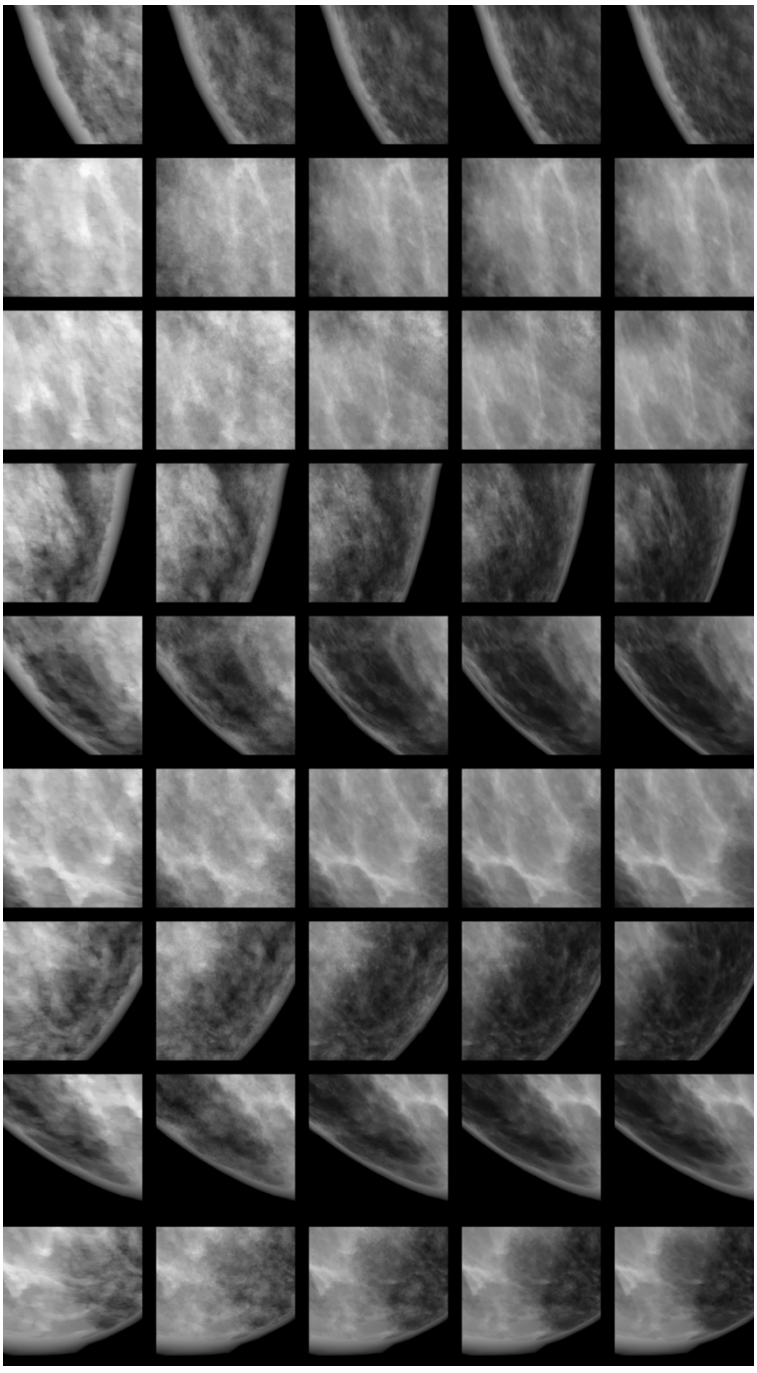
ROI1
ROI2
ROI3
ROI4
ROI5
ROI6
ROI7
ROI8
ROI9
T=0%
T=50%
T=75%
T=95%
T=100%

Figure 8: Effects of binarization threshold. Each row shows the same mammographic ROI with increasing PLN binarization threshold (T). T=0% means all values of PLN were set to 1, i.e., all adipose voxels in the boundary region were changed to glandular, while T=100 means all values of PLN were set to 0, i.e., no PLN was added. The amount of PLN added decreases from left to right.

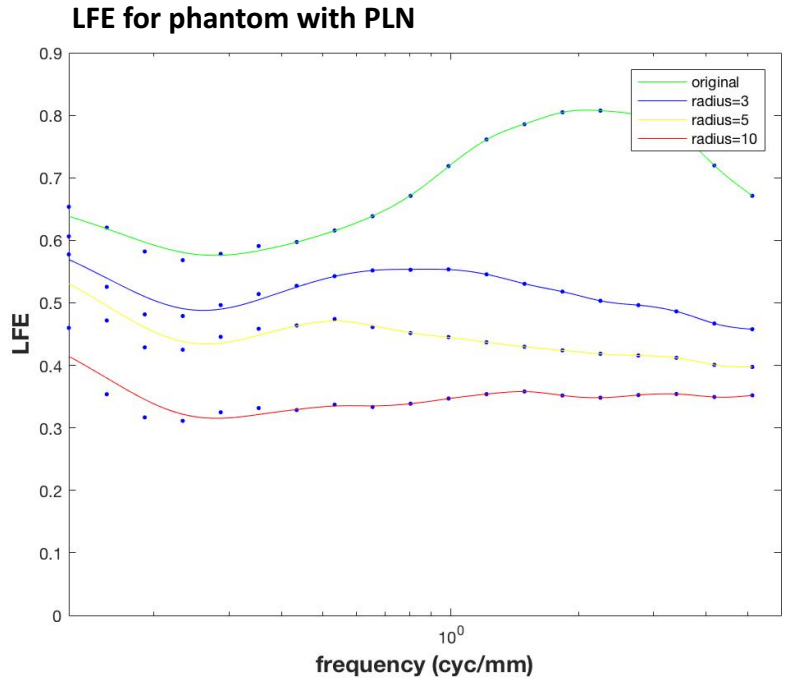

Figure 9: Laplacian fractional entropy (LFE) calculated from simulated mammograms of a phantom with different PLN boundary radius. At each frequency, the value of LFE curve decreased with increasing radius, due to the fact that pure PLN has all zero LFE values.

As the boundary radius increased from 0, 3, 5, up to 10 voxels, the power exponent beta follows a decreasing trend with beta = 3.29, 3.29, 3.27, 3.24 respectively, but did not

have a noticeable change (only 1.2% decrease between original phantom and the one with radius of 10 voxels), whereas LFE changed substantially, which agrees with the visual appearance of ROIs, showing the significance of non-Gaussian statistical properties of breast images.

3.3. Quantitative evaluation

3.3.1 Power spectrum analysis

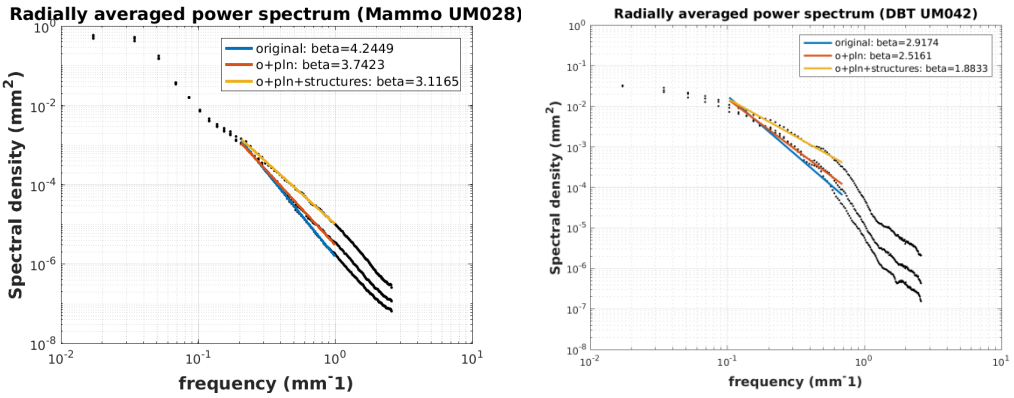

(a) dense fatty

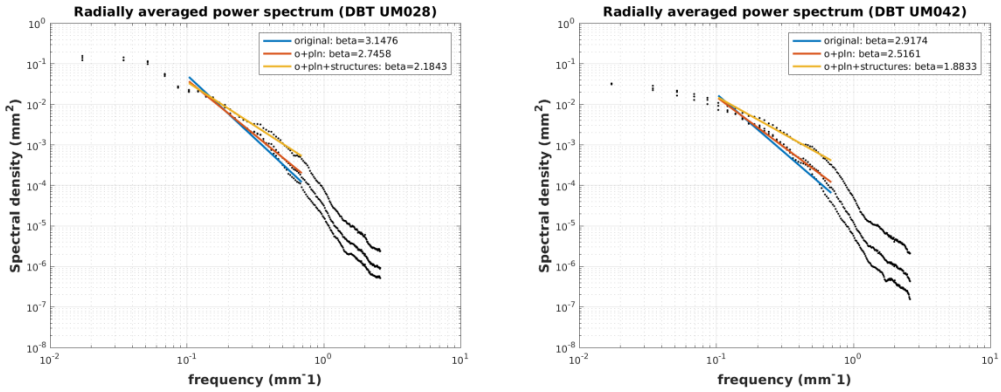

(b) dense fatty

Figure 10: Examples of radially averaged noise power spectrum (NPS) for simulated mammograms and DBT reconstructions of representative dense (left) and fatty (right) breasts. (a) NPS for mammograms at each step of the phantom enhancement including original patient-based phantom (blue line), phantom with PLN (red line), and phantom with both PLN and rule-based anatomical structures (yellow line). (b) NPS for middle slice of DBT reconstructions at each step of the phantom development, displayed in the same way as NPS for mammograms.

Figure 10 plots the radially averaged noise power spectrum (NPS) calculated from simulated mammograms and middle slice of DBT reconstructions through each step of the phantom enhancement, starting from the original patient-based phantom, followed by phantom with power law noise (PLN), and phantom with both PLN and rule-based breast anatomical structures, such as Coopers' ligaments, ductal trees and vessel network. With the addition of these high-frequency details, both the dense and fatty breast showed the same trend of decreasing slope (higher line fit), but the differences were more pronounced for the fatty breast, in which there is a greater volume available for adding structures.

Calculated from mammograms, the average power exponent β of the original phantom is 4.04±0.11, which decreased significantly to 3.51±0.18 for the phantom with PLN (t-test, $p<0.0001$), and again decreased significantly to 2.80±0.14 for the phantom with PLN, Cooper's ligaments, ductal trees and vessels (t-test, $p<0.0001$). The average β values calculated from DBT reconstruction share the same trend, with β=2.91±0.33 for the original phantoms, 2.55 ±0.27 (t-test, $p<0.0001$) for phantoms with PLN, and 1.84 ±0.15 (t-test, $p<0.0001$) for phantoms with PLN and rule-based structures. The continuous decrease in β verifies that high frequency components have been added to the original phantom during each step.

3.3.2 Laplacian fractional entropy (LFE) analysis

LFE for a dense and a fatty breast phantom are shown in Figure 11. In Figure 12, the averaged LFE calculated from all 31 cases are plotted. The LFE curves follow a decreasing trend as PLN, and rule-based breast structures were added to the original phantom. The range and shape of the LFE curve for the completely enhanced phantoms agrees with the curve for real patients' mammograms, indicating the realism of non-Gaussian statistical properties of the enhanced phantoms.

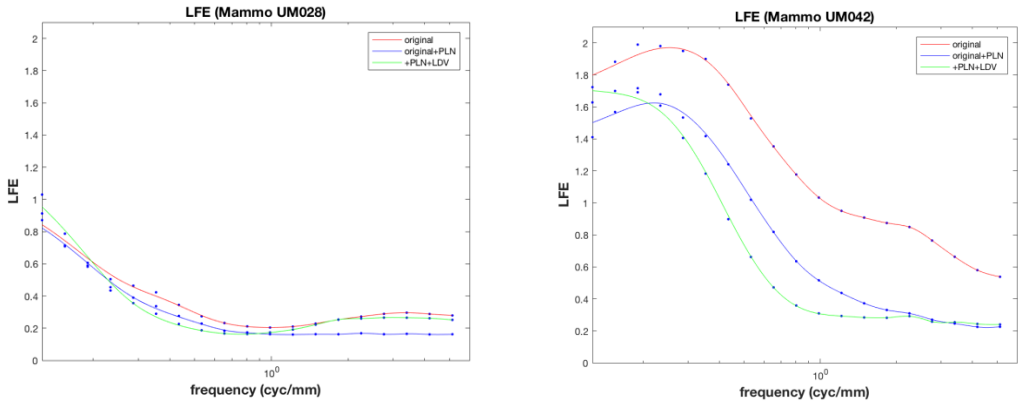

(a) dense (b) fatty

Figure 11: LFE for a dense and a fatty breast.

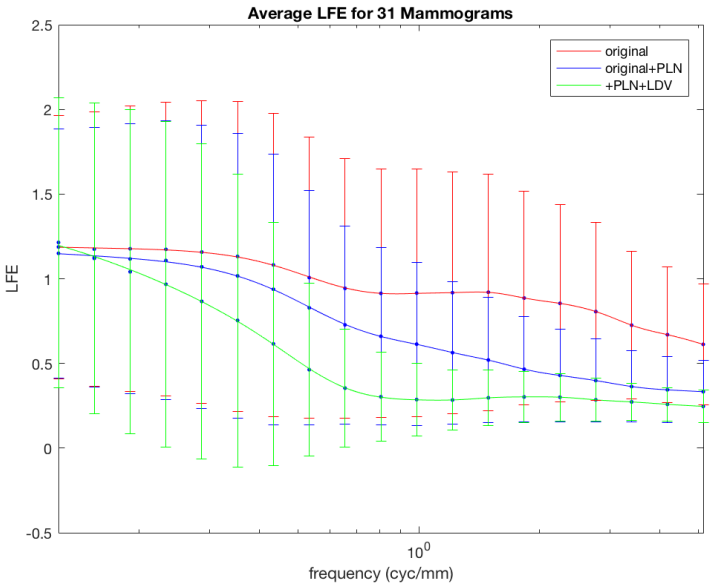

Figure 12: Laplacian fractional entropy (LFE) for each step of phantom enhancement. LFE is plotted as a function of spatial frequency for the original patient-based phantoms, phantoms with power law noise (PLN), and phantom with both PLN and rule-based breast structures. (Error bar shows 1 std.)

3.3.3 Effects of breast density

To assess the effect of breast density, the power exponent beta calculated from simulated mammograms and middle coronal slice of DBT reconstructions are plotted against original breast density in Figure 12 (a) and (b), with red representing the original phantoms, blue showing the phantoms with PLN, and green showing the phantoms with PLN and high frequency breast structures. Each phantom enhancement step constantly decreased the beta for phantoms of all densities. Dense breast phantoms have a slightly higher beta, and the decrease in beta caused by adding PLN is more obvious for fatty

breast phantoms, due to the fact that PLN was added in the adipose region. Therefore, the more adipose tissue a breast phantom contains, the larger decrease in beta it will have after adding PLN. The same trends are shared by both the beta calculated from mammograms and DBT reconstructions.

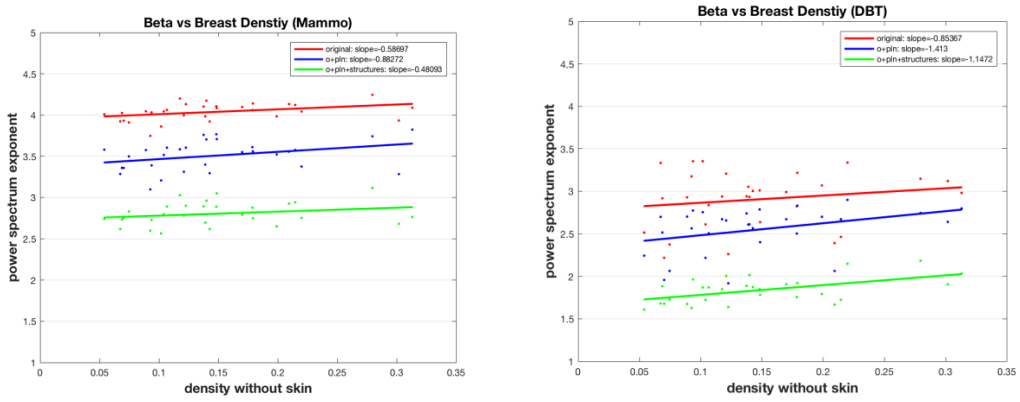

(a) (b)

Figure 13: Power exponent beta against breast density calculated from (a) simulated mammograms and (b) DBT reconstructions.

4. Discussion and Conclusion

Previous development of computational breast phantoms was either through generating pure mathematical models or segmenting real patient images. The former, rule-based approach is flexible, quick and high in resolution, however the result can often lack realism. The patient-based approach, on the other hand, has inherently higher realism, which is essential in breast imaging studies and lesion model studies, nevertheless it has low resolution due to limitations of acquiring and processing human subject data. Therefore, the purpose of this research is to combine the advantages of the two approaches together to create hybrid breast phantoms with inherit realism from patient data that are enhanced in resolution by mathematical models.

The major procedures of phantom enhancement in this research are first to acquire compressed patient-based phantoms that are segmented from breast CT images, then add power-law noise (PLN) at the boundary between glandular and adipose tissue to create high frequency contour of the glandular tissue, and finally fuse high resolution mathematical models of breast structures that are lost during the imaging process, including Cooper's ligaments, ductal trees, and vascular network. Simulated 2D mammograms and 3D DBT volumes visually demonstrated the effects of each procedure

of phantom enhancement. The ability to generate different levels of PLN was demonstrated by controlling parameters such as boundary radius and binarization threshold.

Assessing the realism of phantoms is a very challenging task. In this study, we evaluated two different quantitative metrics that have been reported in the literature. In power spectrum analysis, the decreasing exponent or beta support the hypothesis that high frequency details of breast were added to the patient-based phantoms during each procedure of enhancement. The final enhanced phantoms have averaged beta equals to 2.80 ± 0.14 for simulated mammogram, which falls in the range of beta calculated from real patients' mammogram (2.83 ± 0.35).

While power spectrum evaluates the frequency components of the data, Laplacian fraction entropy (LFE) captures the structural content of the data for a given spatial frequency. Based on the analysis of 26 patients, Abbey *et al.* found that the mammographic images have highest LFE values (70%-90%) at the lowest frequency (0.125 cyc/mm), which then decay as frequency increases. Similar peak value and decay trend was observed in our simulated mammograms of enhanced phantoms.

The power spectrum exponent β of PLN was set to be 3 intentionally to match with the mean β of real mammograms found in literature, which unsurprisingly shift β closer to 3. In the future work, the effects of adding PLN with different β can be explored.

Furthermore, negative PLN that degrades the highest class of glandular can be included in the phantom so as to add high frequencies to the densest glandular and balance the density increase caused by positive PLN. The addition of negative PLN may also improve lesion detectability, since it breaks down the uniform high density glandular.

The rule-based Cooper's ligaments, ductal network, and vascular system were generated separately from the original phantoms. In the future, parameters of these breast structures should be determined by original breast density, and glandular distribution.

The above mentioned improvements may not be fully evaluated by power spectrum analysis or LFE analysis. Therefore, observer study may be required for evaluating realism along the further steps of phantom enhancement.

In conclusion, this first generation of hybrid phantoms were successfully enhanced in high frequency contents by addition of rule-based structures, while inherited realism from patient-based anatomy. The effects of adding PLN as high-frequency contour of glandular, and adding organized structures such as Cooper's ligament, ductal network and vascular system were visually demonstrated by simulated mammograms and DBT reconstructions at every stage, and the difference images between each two stages. Effects of PLN changing parameters were also displayed and compared as mammogram ROIs. Finally, power spectrum analysis and LFE analysis quantitatively validated that both

frequency contents and structure contents of our simulated images were consistent with those calculated from real patients' images.

Reference

[1] V. P. Jackson, R. E. Hendrick, S. A. Feig, and D. B. Kopans, "Imaging of the radiographically dense breast," *Radiology*, vol. 188, no. 2, pp. 297–301, 1993.

[2] M. J. Yaffe, "What should the burden of proof be for acceptance of a new breast-cancer screening technique?," *Lancet*, vol. 364, no. 9440, pp. 1111–1112, 2004.

[3] J. A. Baker and J. Y. Lo, "Breast tomosynthesis. State-of-the-art and review of the literature," *Acad. Radiol.*, vol. 18, no. 10, pp. 1298–1310, 2011.

[4] I. Sechopoulos, "A review of breast tomosynthesis. Part I. The image acquisition process," *Med. Phys.*, vol. 40, no. 1, p. 014301–n/a, Jan. 2013.

[5] I. Sechopoulos, "A review of breast tomosynthesis. Part II. Image reconstruction, processing and analysis, and advanced applications," *Med. Phys.*, vol. 40, no. 1, p. 014302–n/a, Jan. 2013.

[6] P. Skaane *et al.*, "Comparison of Digital Mammography Alone and Digital Mammography Plus Tomosynthesis in a Population-based Screening Program," *Radiology*, vol. 267, no. 1, pp. 47–56, Apr. 2013.

[7] F. SM, R. EA, R. SL, and et al, "Breast cancer screening using tomosynthesis in combination with digital mammography," *JAMA*, vol. 311, no. 24, pp. 2499–2507, Jun. 2014.

[8] J. M. Lewin, P. K. Isaacs, V. Vance, and F. J. Larke, "Dual-energy contrast-enhanced digital subtraction mammography: Feasibility," *Radiology*, vol. 229, no. 1, pp. 261–268, 2003.

[9] R. A. Jong *et al.*, "Contrast-enhanced digital mammography: Initial clinical experience," *Radiology*, vol. 228, no. 3, pp. 842–850, 2003.

[10] K. K. Lindfors, J. M. Boone, T. R. Nelson, K. Yang, A. L. C. Kwan, and D. F. Miller, "Dedicated breast CT: Initial clinical experience," *Radiology*, vol. 246, no. 3, pp. 725–733, 2008.

[11] J. M. Boone, T. R. Nelson, K. K. Lindfors, and J. A. Seibert, "Dedicated Breast CT: Radiation Dose and Image Quality Evaluation," *Radiology*, vol. 221, no. 3, pp. 657–667, Dec. 2001.

[12] N. D. Prionas *et al.*, "Contrast-enhanced dedicated breast CT: Initial clinical experience," *Radiology*, vol. 256, no. 3, pp. 714–723, 2010.

[13] A. O'Connell *et al.*, "Cone-Beam CT for Breast Imaging: Radiation Dose, Breast Coverage, and Image Quality," *Am. J. Roentgenol.*, vol. 195, no. 2, pp. 496–509, Aug. 2010.

[14] R. L. McKinley, M. P. Tornai, L. A. Tuttle, D. Steed, and C. M. Kuzmiak, "Development and Initial Demonstration of a Low-Dose Dedicated Fully 3D Breast CT System BT - Breast Imaging: 11th International Workshop, IWDM 2012, Philadelphia, PA, USA, July 8-11, 2012. Proceedings," A. D. A. Maidment, P. R. Bakic, and S. Gavenonis, Eds. Berlin, Heidelberg: Springer Berlin Heidelberg, 2012, pp. 442–449.

[15] P. R. Bakic, M. Albert, D. Brzakovic, and A. D. A. Maidment, "Mammogram synthesis using a 3D simulation. I. Breast tissue model and image acquisition simulation," *Med. Phys.*, vol. 29, no. 9, pp. 2131–2139, 2002.

[16] P. R. Bakic, M. Albert, D. Brzakovic, and A. D. A. Maidment, "Mammogram synthesis using a 3D simulation. II. Evaluation of synthetic mammogram texture," *Med. Phys.*, vol. 29, no. 9, pp. 2140–2151, 2002.

[17] P. R. Bakic, M. Albert, D. Brzakovic, and A. D. A. Maidment, "Mammogram synthesis using a three-dimensional simulation. III. Modeling and evaluation of the breast ductal network," *Med. Phys.*, vol. 30, no. 7, pp. 1914–1925, 2003.

[18] B. A. Lau, I. Reiser, R. M. Nishikawa, and P. R. Bakic, "A statistically defined anthropomorphic software breast phantom," *Med. Phys.*, vol. 39, no. 6, pp. 3375–3385, 2012.

[19] C. G. Graff, " A new, open-source, multi-modality digital breast phantom ," 2016, vol. 9783, pp. 978309–978310.

[20] P. R. Bakic, C. Zhang, and A. D. A. Maidment, "Development and characterization of an anthropomorphic breast software phantom based upon region-growing algorithm," *Med. Phys.*, vol. 38, no. 6, pp. 3165–3176, 2011.

[21] K. Bliznakova, S. Suryanarayanan, A. Karellas, and N. Pallikarakis, "Evaluation of an improved algorithm for producing realistic 3D breast software phantoms: Application for mammography," *Med. Phys.*, vol. 37, no. 11, pp. 5604–5617, 2010.

[22] B. Chen *et al.*, "An Anthropomorphic Breast Model for Breast Imaging Simulation and Optimization," *Acad. Radiol.*, vol. 18, no. 5, pp. 536–546, 2011.

[23] J. Näppi, P. B. Dean, O. Nevalainen, and S. Toikkanen, "Algorithmic 3D simulation of breast calcifications for digital mammography," *Comput. Methods Programs Biomed.*, vol. 66, no. 1, pp. 115–124, 2001.

[24] D. D. Pokrajac, A. D. A. Maidment, and P. R. Bakic, "Optimized generation of high resolution breast anthropomorphic software phantoms," *Med. Phys.*, vol. 39, no. 4, pp. 2290–2302, 2012.

[25] P. Taylor, R. Owens, and D. Ingram, "Simulated mammography using synthetic 3D breasts," *Digit. Mammogr.*, pp. 283–290, 1998.

[26] P. Elangovan, D. R. Dance, K. C. Young, and K. Wells, " Generation of 3D synthetic breast tissue ," 2016, vol. 9783, pp. 978306–978308.

[27] C. Hoeschen, U. Fill, M. Zankl, W. Panzer, D. Regulla, and W. Döhring, "A high-resolution voxel phantom of the breast for dose calculations in mammography," *Radiat. Prot. Dosimetry*, vol. 114, no. 1–3, pp. 406–409, 2005.

[28] J. M. O'Connor, M. Das, C. S. Dider, M. Mahd, and S. J. Glick, "Generation of voxelized breast phantoms from surgical mastectomy specimens," *Med. Phys.*, vol. 40, no. 4, 2013.

[29] C. M. Li, W. P. Segars, G. D. Tourassi, J. M. Boone, and J. T. Dobbins, "Methodology for generating a 3D computerized breast phantom from empirical data," *Med. Phys.*, vol. 36, no. 7, pp. 3122–3131, 2009.

[30] W. P. Segars *et al.*, "Population of 100 realistic, patient-based computerized breast phantoms for multi-modality imaging research," in *Progress in Biomedical Optics and Imaging - Proceedings of SPIE*, 2014, vol. 9033.

[31] D. W. Erickson *et al.*, "Population of 224 realistic human subject-based computational breast phantoms," *Med. Phys.*, vol. 43, no. 1, pp. 23–32, Jan. 2016.

[32] G. M. Sturgeon, N. Kiarashi, J. Y. Lo, E. Samei, and W. P. Segars, "Finite-element modeling of compression and gravity on a population of breast phantoms for multimodality imaging simulation," *Med. Phys.*, vol. 43, no. 5, pp. 2207–2217, May 2016.

[33] G. M. Sturgeon *et al.*, " Eigenbreasts for statistical breast phantoms ," 2016, vol. 9783, p. 97832B–97832B–9.

[34] S.-Y. Huang *et al.*, "The characterization of breast anatomical metrics using dedicated breast CT," *Med. Phys.*, vol. 38, no. 4, pp. 2180–2191, 2011.

[35] M. J. Yaffe *et al.*, "The myth of the 50-50 breast," *Med. Phys.*, vol. 36, no. 12, pp. 5437–5443, 2009.

[36] A. E. Burgess, F. L. Jacobson, and P. F. Judy, "Human observer detection experiments with mammograms and power-law noise," *Med. Phys.*, vol. 28, no. 4, pp. 419–437, Apr. 2001.

[37] A. P. Cooper, "No Title," *Anat. Breast*, 1840.

[38] P. R. Bakic, D. D. Pokrajac, R. Caro, and A. D. A. Maidment, "Breast imaging: 12th international workshop, iwdm 2014, gifu city Japan, June 29-July 2, 2014," *Proceedings] Ch. Real Istic Simul. Breast Tissue Microstruct. Softw. Anthr. Phantoms*, pp. 348–355, 2014.

[39] R. Zeng, S. Park, P. Bakic, and K. J. Myers, “Evaluating the sensitivity of the optimization of acquisition geometry to the choice of reconstruction algorithm in digital breast tomosynthesis through a simulation study,” *Phys. Med. Biol.*, vol. 60, no. 3, p. 1259, 2015.

[40] N. Kiarashi *et al.*, “Development of realistic physical breast phantoms matched to virtual breast phantoms based on human subject data,” *Med. Phys.*, vol. 42, no. 7, pp. 4116–4126, Jul. 2015.

[41] L. Cockmartin, H. Bosmans, and N. W. Marshall, “Comparative power law analysis of structured breast phantom and patient images in digital mammography and breast tomosynthesis,” *Med. Phys.*, vol. 40, no. 8, 2013.

[42] C. K. Abbey, P. R. Bakic, D. D. Pokrajac, A. D. A. Maidment, M. P. Eckstein, and J. M. Boone, “Non-Gaussian statistical properties of virtual breast phantoms,” in *SPIE Medical Imaging*, 2014, p. 90370G–90370G.